analytical chemistry

pubs.acs.org/ac Article

A Photoresponsive and Metal−Organic Framework Encapsulated DNA Tetrahedral Entropy-Driven Amplifier for High-Performance Imaging Intracellular MicroRNA

Jia-Ling Gao,[§] Liu Yuheng,[§] Jun-Xian Liu, Hong-Wu Tang, and Cheng-Yu Li*

Cite This: *Anal. Chem.* 2021, 93, 16638−16645 Read Online

ACCESS | Metrics & More | Article Recommendations | Supporting Information

ABSTRACT: The further development of high-performance fluorescent biosensors to image intracellular microRNAs is beneficial to cancer medicine. By virtue of the need for enzymes and hairpin DNA probes, the entropy-driven reaction-assisted signal amplification strategy has shown an enormous potential to accomplish this task. Nevertheless, this good option still meets with poor biostability, low cell uptake efficiency, and unsatisfactory accuracy. On the basis of these challenges, we put forward here a battery of solving pathways. First, the straight DNA probes are anchored onto the vertexes of dual DNA tetrahedrons, and thus the enzyme resistance of the whole sensing system is observably enhanced. A metal−organic framework (ZIF-8 nanoparticle), which can be effectively dissociated into a weakly acidic environment, then is employed as an additional delivery vehicle to encapsulate such a DNA tetrahedron sustained biosensor and finally bring about a more efficient endocytosis. Last, a kind of photocleavage-linker triggered photoresponsive manner is incorporated to achieve an exceptional precise target identification, by which the biosensor can only be initiated under the irradiation of an externally mild 365 nm ultraviolet light source. In accordance with the above efforts, worthy assay performance toward microRNA-196a has given rise to this newly constructed biosensor, whose sensitivity is down to 2.7 pM and also able to distinguish single-base variation. Beyond that, the amplifier can work as a powerful imaging toolbox to accurately determine the targets in living cells, providing a promising intracellular sensing platform.

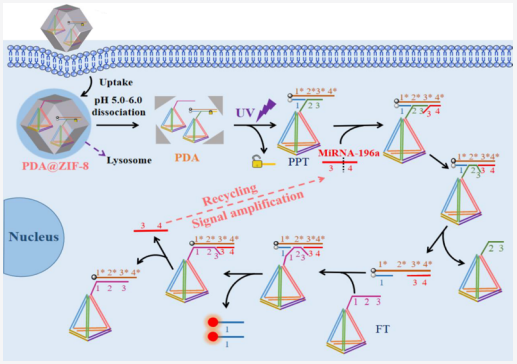

INTRODUCTION

Until now, the excess or loss of small noncoding microRNAs (miRNAs, whose base numbers are only 22−25 nt) has been demonstrated to present a fairly high relevance to the progression of malignant tumors.[1−3] Thus, constructing a sensitive detection method, especially at the cellular level, is of necessity to offer useful information for the clinical treatment of cancer diseases. To realize this aim, plentiful biosensing platforms (e.g., colorimetry,[4,5] electrochemistry,[6−8] and fluorescence[9−12]) have been developed. Comparatively, more attention has been paid to the fluorescent biosensors that can directly image living cells. Because the intracellular contents of miRNAs are relatively low, many signal amplification strategies including rolling circle amplification,[13,14] catalytic hairpin assembly,[15−17] entropy-driven reaction,[18,19] and hybridization chain reaction[20−22] are commonly integrated to further improve the imaging sensitivity. Benefiting from the needless of enzymes and hairpin DNA probes, the entropy-driven mechanism is endowed with a higher reaction efficiency. Although this sound amplifier is promising to detect intracellular miRNAs, it still suffers from a series of challenges.

First, due to the fact that the cell itself is a very complex medium, the stable existence of the straight DNA probes initiating the entropy-driven reaction is a primary consideration. In particular, the widely distributed nucleases in cells are probably to make a distinct degradation phenomenon to these exogenous sources, leading to a poor signal amplification effect and even false signals.[23] As a result, exploring an effective protection approach for such a DNA molecule programmed fluorescent biosensor is of great significance. Along with the discovery of a number of emerging DNA nanostructures, a kind of rigid skeleton, DNA tetrahedron, is promising to address this concern.[24−27] Typically, the tetrahedral skeleton is formed by a simple annealing process, and it can work as a solid snail's shell[24] to observably enhance the enzyme resistance of the vertex-anchored nucleic acid chains.

Despite that the combination of DNA tetrahedron is a desired choice, its negatively charged property can produce a strong electrostatic repulsion with the cell membrane, resulting in a difficulty for this pure DNA carrier to enter into the cytoplasm.[28] Therefore, it is indispensable to couple a more

Received: September 21, 2021
Accepted: November 23, 2021
Published: December 2, 2021

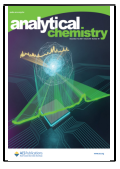

https://doi.org/10.1021/acs.analchem.1c04105
Anal. Chem. 2021, 93, 16638−16645

Scheme 1. (A) Preparation Steps of Photoresponsive DNA Tetrahedral Amplifier (PDA) and Its ZIF-8 Encapsulation (PDA@ZIF-8); and (B) Cell Uptake and Delivery Pathway of PDA@ZIF-8-Supported Fluorescent Biosensor and Its Workflow in Living Cells

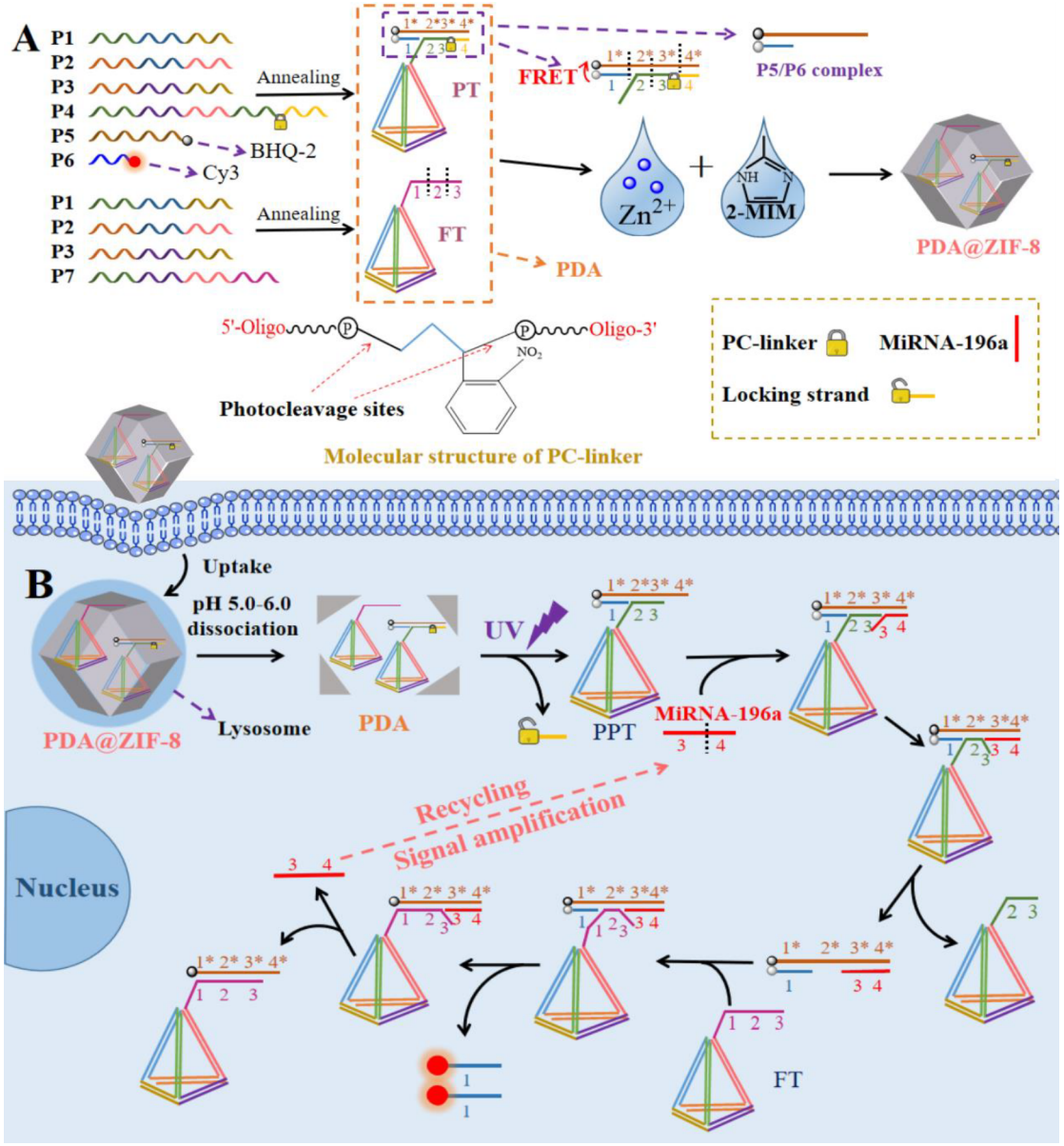

efficient delivery vehicle to boost the efficiency of cell uptake. With the rapid progress of material science, a class of frequently applied porous nanomaterials, metal−organic frameworks (MOFs), can well overcome this drawback.[29−32] Generally, MOFs are fabricated by a traditional metal ions-based coordination chemistry, and their tunable hollow structure is able to further store biomolecules. By means of the valid nonspecific adsorption capacity of cell membrane to nanoparticles, the employment of MOFs is conducive to the endocytosis of DNA tetrahedron-supported biosensors.[31] Moreover, a majority of MOFs are easily dissociated in a weak acid environment, and their internally loaded sensing elements can be perfectly released upon being taken up by the lysosome and delivered into the cytoplasm.[32]

More than these, by reason for the essential complementary pairing to achieve target identification, another problem is that the extensively existed miRNAs in cell medium will beforehand trigger the designed sensing route during the whole intracellular delivery. In such an inevitable situation, the final captured fluorescence signals (at the position where the biosensors reach) cannot truly reflect to the target content, bringing about an unsatisfactory sensing accuracy.[33] Hence, seeking a pathway to break through this bottleneck is also pivotal. Fortunately, a photoresponsive sensing concept is primely to fulfill this goal. In practical application, the biosensors are introduced with a photocleavage (PC)-linker, and they can be manually initiated with the assistance of an external light source [normally in ultraviolet (UV) range)]. Recently, some advanced studies have certified the feasibility of this photoactivation manner and extended it to carry out intracellular sensing with exceptional precision.[34−36]

In response to the aforementioned issues, for the first time, we propose a dual DNA tetrahedrons sustained entropy-driven amplifier wherein an external light source and a metal−organic

https://doi.org/10.1021/acs.analchem.1c04105
Anal. Chem. 2021, 93, 16638−16645

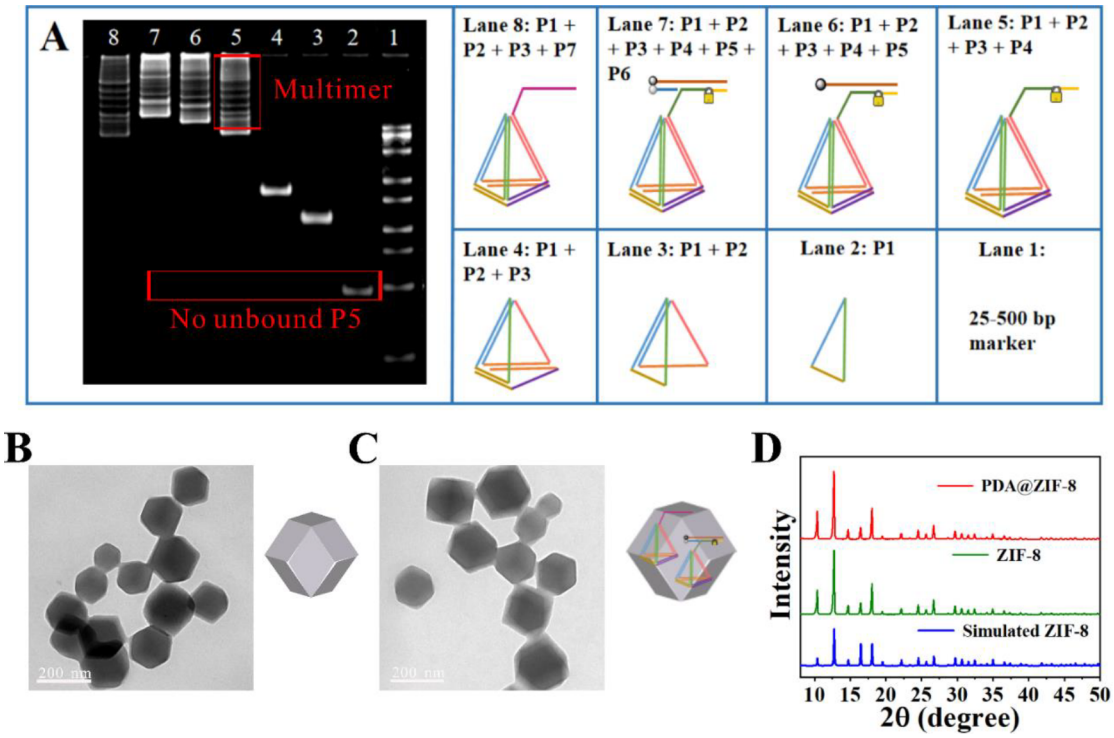

Figure 1. (A) 10% PAGE verification of successful preparations of PT and FT. (B) TEM image (scale bar is 200 nm) of pure ZIF-8. (C) TEM image (scale bar is 200 nm) of PDA@ZIF-8. (D) XRD patterns of PDA@ZIF-8, pure ZIF-8, and simulated ZIF-8.

framework are employed to realize precise target identification and improve the endocytosis efficiency, respectively, and apply this new fluorescent biosensor as an efficient imaging toolbox to sensitively determine miRNA-196a, a kind of potential next-generation lung cancer associated biomarker,[37] in living cells. Scheme 1A shows the preparation steps of this photo-responsive DNA tetrahedral amplifier (denoted as PDA) under the encapsulation of ZIF-8 nanoparticles (detailed nucleic acid sequences can be found in Table S1), and its concrete workflow in cell medium is exhibited in Scheme 1B. To be specific, the PDA is composed of a photoresponsive tetrahedron (denoted as PT) and a fuel tetrahedron (denoted as FT). The former is fabricated by self-assembling six single-stranded DNA chains (P1, P2, P3, P4, P5, and P6) through a convenient annealing treatment. For the vertex of the formed tetrahedral structure, the P4 chain is extended out a PC-linker modified locking strand (4 domain), and it is further hybridized with the P5/P6 complex. In this case, the very proximate Cy3 and BHQ-2 molecules will appear as a significant fluorescence quenching phenomenon because of the Förster resonance energy transfer (FRET) effect. In the same way, the FT with a skeleton similar to that of the PT is assembled from four single-stranded DNA chains (P1, P2, P3, and P7), of which the prolonged portion of the P7 chain ("1 + 2 + 3" domain) is perfectly matched with part of the P5 chain ("1* + 2* + 3*" domain). Next, the FT and the PT are encapsulated together into a ZIF-8 nanoparticle (denoted as PDA@ZIF-8) via a coordination chemistry between 2-methylimidazole (2-MIM) and Zn^{2+}.

When a cellular lysosome endocytoses the as-prepared nanocomposite, its weak acid environment (pH 5.0−6.0) will effectually dissociate the ZIF-8 nanoparticle to discharge the internal PDA to evenly distribute into the cytoplasm. With irradiation of the cell with a UV light at 365 nm, the connection ends of the PC-linker are effectively cleaved to release the locking strand (the product is indicated as PPT), and the expected entropy-driven reaction is finally initiated. In the presence of miRNA-196a ("3 + 4" domain), the target first binds to the exposed 4* domain of the PPT and then triggers a successive strand displacement process to form the P5/P6/target complex. After that, the exposed 2* domain combines with the vertex chain of the FT to touch off a second round of strand displacement procedures. At the moment, not only does the released P6 chain make the Cy3 molecule stay away from the BHQ-2 molecule to strongly recover the as-quenched fluorescence signals, but also the dissociative target can perform the next cycle of the entropy-driven reaction to achieve effective signal amplification.

EXPERIMENTAL SECTION

Preparation of PDA. For the preparation of PT, the P1, P2, P3, P4, P5, and P6 chains with identical molar weights (100 nmol) were first mixed together via a vortex in a 1.5 mL tube and then added with certain amounts of Tris buffer solution (20 mM Tris-base, 50 mM $MgCl_2$, pH 8.0) to regulate the total DNA concentration at 2 μM. After transferring the stock solution into a 95 °C water bath and further maintaining the temperature for 10 min, we immediately put it to rest in a −20 °C refrigerator for another 10 min. The same procedures were employed for the preparation of FT, of which the molar weights of the P1, P2, P3, and P7 chains were also 100 nmol. The final PDA was obtained by fully mixing the PT and the FT in another 1.5 mL tube, and it was kept in a 4 °C refrigerator for subsequent use.

Preparation of PDA@ZIF-8. At first, 18.6 mg of $Zn(NO_3)_2{\cdot}6H_2O$ was dissolved into 0.5 mL of methanol solution via ultrasonic processing, followed by the introduction of 50 nmol of PDA to form solution **I**. Next, 10.3 mg of 2-

https://doi.org/10.1021/acs.analchem.1c04105
Anal. Chem. 2021, 93, 16638−16645

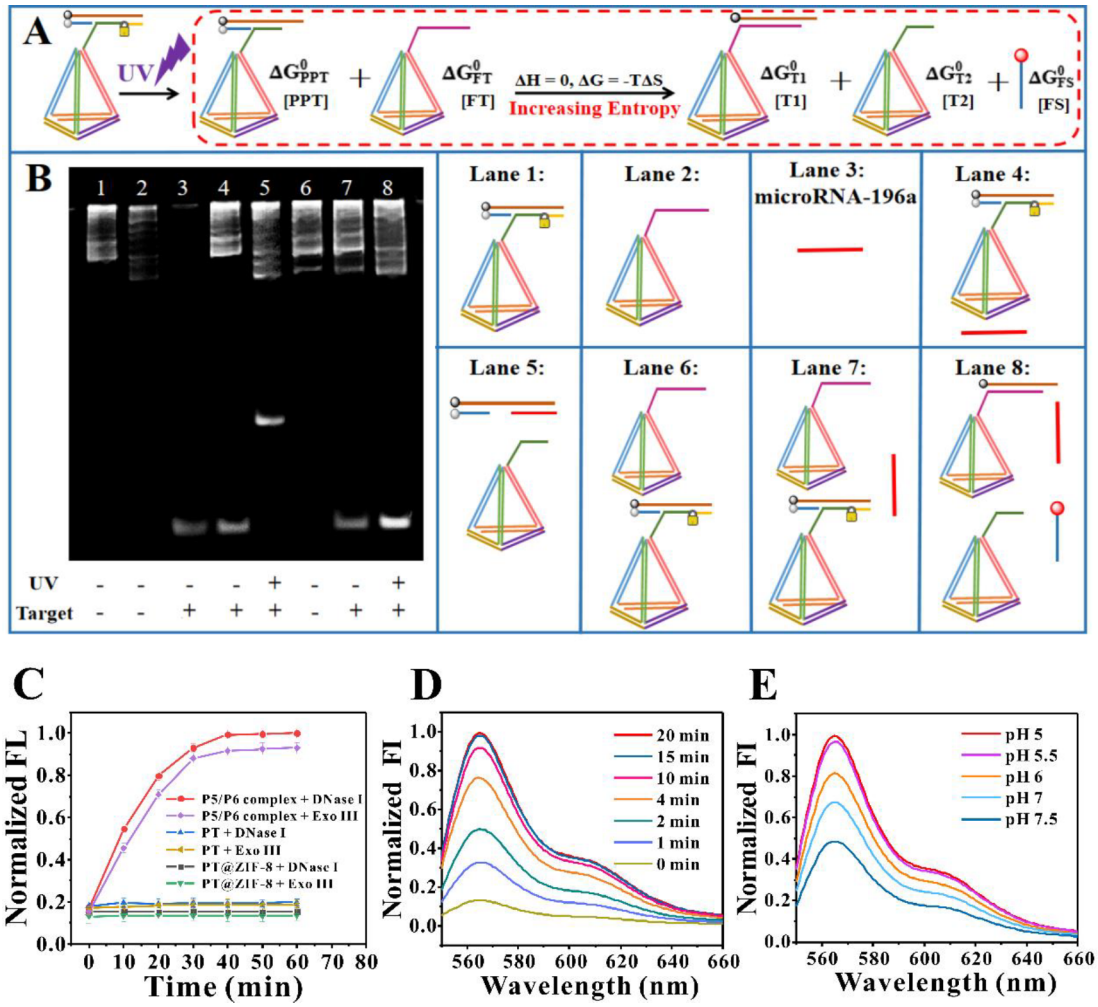

Figure 2. (A) Reaction equation (all objects are marked with corresponding parameters) of the photoresponsive entropy-driven system under the support of dual DNA tetrahedrons. (B) Practical feasibility (10% PAGE experiment) of the proposed reaction in (A). (C) Enzyme resistance of the DNA tetrahedral skeleton and its multimer under the treatments of high concentration (8 U/mL) DNase I and Exo III. FI indicates the abbreviation of fluorescence intensity. (D) Optimizing photoresponsive time by using a PDA-supported fluorescent biosensor. (E) Optimizing pH discharge condition by using a PDA@ZIF-8-supported fluorescent biosensor under the optimal 365 nm UV light irradiation time.

MIM was dissolved into another 0.5 mL of methanol solution via ultrasonic processing to form solution **II**. Subsequently, solution **II** was added into solution **I** drop-by-drop within 1 min, and the mixture was further incubated at 37 °C with gentle shaking. Once the original clear solution was transformed into a turbid state, the residual PDAs were removed by treating with centrifugation (10 000 rpm) for 10 min. Finally, the collected PDA@ZIF-8 was washed twice with ultrapure water and kept in a 4 °C refrigerator for subsequent use.

Using PDA@ZIF-8-Supported Fluorescent Biosensor to Image Intracellular miRNA-196a. A549 and HeLa cells were first grown in 35 mm culture dishes for 24 h (37 °C and 5% CO_2) and then washed twice with 1 × PBS solution (pH 7.4), followed by introduction with the optimal PDA@ZIF-8 (30 μg/mL). After treatment with the 365 nm UV light irradiation for 15 min (power densities are 3.2 W/cm^2 for both cases) during the first 2 h of incubation time in a thermostatic incubator, the cells are left to continue to rest for another 2 h. By further removing the residual PDA@ZIF-8 through the 1 × PBS solution washing, we transferred the culture dishes to a confocal microscope to perform fluorescence imaging.

RESULTS AND DISCUSSION

To begin with, the successful preparations of PT and FT are verified by 10% polyacrylamide gel electrophoresis (PAGE) experiments, and the results are exhibited in Figure 1A. Because the gradual introduction of the nucleic acid chains (P1, P1 + P2, P1 + P2 + P3, and P1 + P2 + P3 + P4) can cause an obvious increase in molecular mass, a markedly shorter migration distance (lanes 2−5) appears during the formation of the tetrahedral skeleton of PT. When the P5 and the P6 chains are further bound onto the vertex of this self-assembled case, the migration rate will progressively become slower (lanes 6 and 7). Because of the fewer bases on the vertex of FT, its migration ability is slightly faster than that of the PT. These distinct differences (other bands with significantly higher molecular masses in lanes 5−8 are attributed to the extra formation of multimer, which can be proved by the atomic force microscopy images in Figure S1) can well demonstrate that the two DNA tetrahedrons can be easily obtained via the adopted annealing treatment.

After that, a classical metal ions-based coordination chemistry is conducted to conjointly encapsulate the as-prepared PT and FT into ZIF-8 nanoparticles. It is clearly

https://doi.org/10.1021/acs.analchem.1c04105
Anal. Chem. 2021, 93, 16638−16645

observed from the transmission electron microscopy (TEM) images (Figure 1B and C) that the encapsulation processing owns a good dispersibility and a hexagonal-like shape similar to that of the pure ZIF-8 nanoparticles, along with neglectable size variations to the statistical histograms (n = 200, mean particle sizes are ∼120 nm for both cases, Figure S2), indicating that the internally loaded DNA nanostructures will not affect the crystal conformation property of the ZIF-8 framework. Such speculation is further proved by the X-ray diffraction (XRD) data (Figure 1D), wherein no other impure diffraction signs are presented in the pattern of PDA@ZIF-8 and all of its featured lines can faultlessly be assigned to the simulated ZIF-8 nanoparticle. The particular elemental map of this nanocomposite is visibly confirmed by the energy dispersive spectroscopy analysis (Figure S3), for which a new signal deriving from the phosphorus in nucleic acids arises to the PDA@ZIF-8, and this finding is also demonstrated by the elemental binding energy (Figure S4). Although no noteworthy changes occur in the hydrate particle sizes after this coordination reaction is fulfilled (Figure S5A), an arresting decline tendency happens to the zeta potentials (decreasing from −13.69 to −21.08 mV, Figure S5B) on account of the negatively charged truth of the DNA molecules. Of note, there are no apparent fluctuations in the thermal stabilities of PDA and PDA@ZIF-8 as well (Figure S6). By selecting a model PT that is not modified with BHQ-2 in the P5 chain, we can acquire that the encapsulation efficiency is as high as 97.7% via the fluorescent inspection (Figure S7).

With assistance of the reliable thermokinetic result (the reaction equation and the definite calculation procedures are presented in Figure 2A and the Supporting Information, respectively), we subsequently take advantage of the PAGE study to examine the practical feasibility of this photoresponsive effect in the presence of miRNA-196a. As can be found in Figure 2B, a complete silent manner (no strand displacement phenomenon) happens to the PT without the introduction of the 365 nm UV light (lane 4). In sharp contrast, a new band attributed to the P5/P6/target complex stemming from the cleavage of the PC-linker (the photocleavage is certified by a convenient duplex model, Figure S8) is exhibited upon irradiating with this light source (lane 5). Moreover, the expected cross reaction between PT and FT is also validated. By reason for the completeness of the locking strand, miRNA-196a alone cannot realize this response (lanes 6 and 7), while a band containing both the FS and the target (because these two chains differ by only one base) that is brighter than the original miRNA-196a appears in the coexistence of this activation light (lane 8), suggesting that the miRNA-196a can be effectively released from the entropy-driven system (not affected by the presence of multimer) to participate in the cyclic design.

Despite that the incorporation of the DNA tetrahedral skeleton is an ideal option for enhancing the enzyme resistance of DNA amplifiers, we still testify the actual stability of PT under the treatments of DNase I and Exo III, the most widespread endonuclease and exonuclease in biological media,[38] respectively. When the individual incubation concentration reaches up to 8 U/mL (much higher than the intracellular condition), it is seen from Figure 2C that gradually elevated background signals are presented to the pure P5/P6 complex with the increase of incubation time, manifesting that such a simple double chain structure occurs a distinct degradation. However, very weak Cy3 emissions are detectable under these circumstances, and this comparative result can primely illustrate that the tetrahedral skeleton and its multimer do protect their vertex-anchored nucleic acid chains (the relevant integrities of PT are simultaneously testified by the 10% PAGE test, Figure S9). Except for this interesting finding, the further encapsulation of ZIF-8 nanoparticles will maintain the outstanding enzyme resistance.

According to our workflow, the 365 nm UV light irradiation is a prerequisite for implementing the subsequent target identification, and the optimization of this issue is of great importance to ensure the best sensing performance. For this reason, the PDA-supported fluorescent biosensor (in the presence of miRNA-196a) is inspected by the introduction of different irradiation times (power densities are as low as 3.2 W/cm^2). As can be seen in Figure 2D, the biosensor shows a remarkable time-dependent behavior, and it will reach a balance point after 15 min of irradiation, implying that a maximum of locking strands are released to ultimately achieve the strongest Cy3 signal recovery. Meanwhile, it is worth pointing out that the same kind of coexistence effect to the UV light and the target is demonstrated in this fluorescent study (Figure S10).

Except for the photoresponsive time, another crucial factor is whether the pH value of lysosome can guarantee the dissociation of ZIF-8 nanoparticles to discharge sufficient PDA. Thus, we further explore the influence of pH condition by examining the PDA@ZIF-8-supported fluorescent biosensor under the optimal irradiation time. The results are displayed in Figure 2E, from which the neutral pH values lead to a much weaker Cy3 emission, uncovering that less ZIF-8 nanoparticles are dissociated in these cases. On the contrary, the weakly acidic pH is more beneficial to the discharge event, whereby the recovered fluorescence intensity will reach a plateau when the pH value is at 5.5, staying consistent with the lysosome environment.

On the strength of these convincing foundations, the extracellular assay performance in buffer solution is being studied by using the PDA-supported fluorescent biosensor. In the absence of the ZIF-8 nanoparticles aided discharge process (Figure S11A), we can acquire that the Cy3 fluorescence is restored inch-by-inch with the incremental addition of miRNA-196a (the target concentrations are from 0 to 20 nM) under the optimal UV light treatment (Figure S11B). After seeking the possible relationship between the target concentration and the signal recovery ratio [represented as $(F - F_0)/F_0$, where F and F_0 denote the fluorescence intensity with and without the introduction of miRNA-196a, respectively], we obtained that the logarithm of the former shows a good linear correlation (R^2 value is 0.9903, Figure S11C) to the latter within a wide concentration range (from 5 pM to 20 nM, spanning through 4 orders of magnitude). In line with the normative calculation formula (three standard deviation of blank samples divided by the slope), it further comes to follow that the limit of detection (LOD) can be estimated to be ∼2.9 pM, reflecting that a very satisfying sensitivity not only meets the requirement of intracellular detection but also holds an overt working superiority in living cells over other recently developed miRNA fluorescent biosensors (Table S2).

Aside from the examination of assay sensitivity, we then roundly attest the specificity due to the high homology of miRNA families.[3] For this purpose, the newly constructed biosensor is first applied to response mismatching targets. In Figure S11D, profiting from the trigger strictness of the strand

https://doi.org/10.1021/acs.analchem.1c04105
Anal. Chem. 2021, 93, 16638−16645

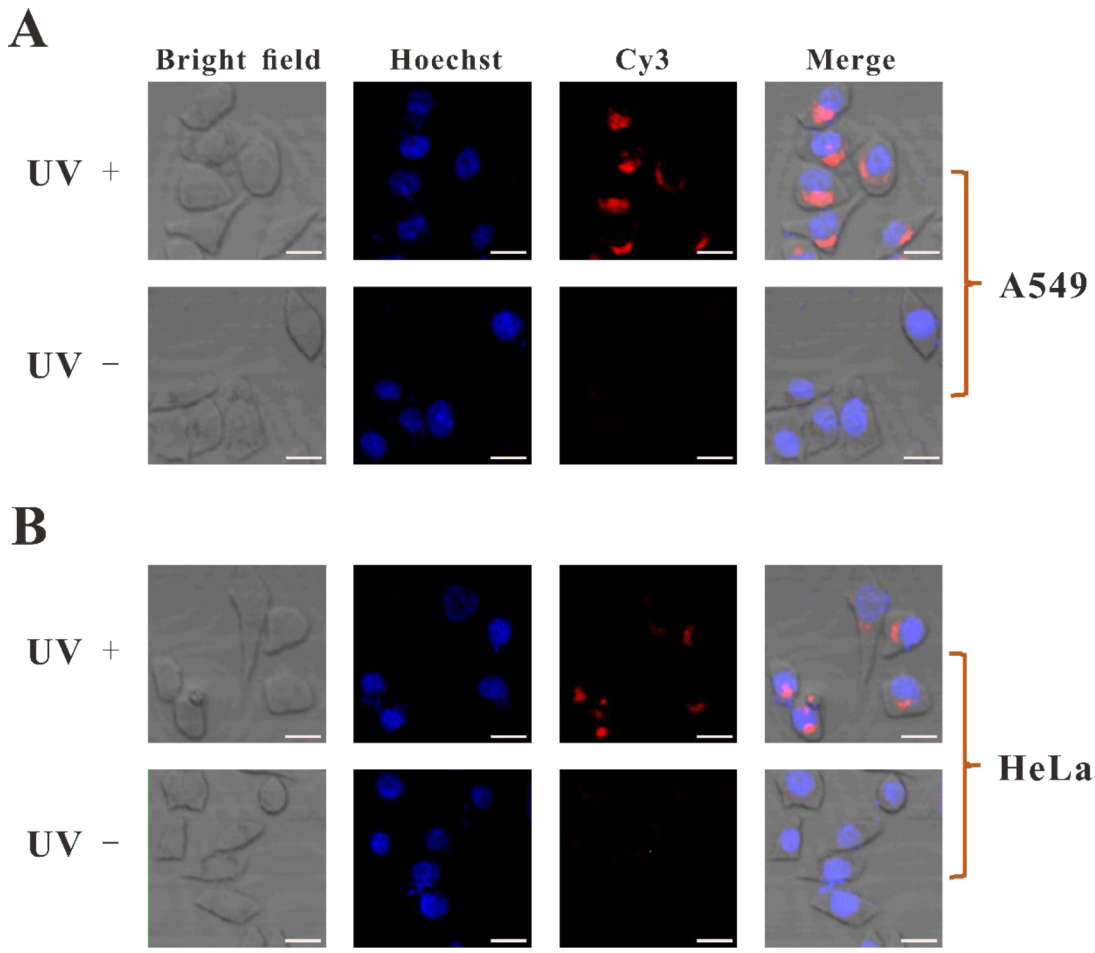

Figure 3. Confocal images of 30 μg/mL PDA@ZIF-8 incubated A549 (A) and HeLa cells (B) in the presence (top images) and absence (bottom images) of 365 nm UV light irradiation. Scale bars, exposure time (Cy3 emission), and signal acquisition channel (Cy3 emission) are 10 μm, 250 ms, and 620 ± 40 nm, respectively.

displacement principle, it is found that a tapering trend of the recovery ratio is rendered to the increased number of mismatched bases. Specifically, the presence of target owns the most notable signal recovery phenomenon (P value < 0.001), whereas the proportion data to this group for single-base, two-base, and three-base mismatched cases (indicated as M1, M2, and M3) observably dropped to 37% (P value < 0.01), 20% (P value < 0.01), and 12% (P value < 0.5), respectively. Considering that numerous interfering biomolecules in cell medium may adversely impact the signal output, additional random RNA (R) and human proteins (cardiac troponin I, carcinoembryonic antigen, and immunoglobulin G) as well as some widespread small molecules (adenosine 5′-triphosphate, Na^+, and K^+) are further investigated. Satisfactorily, these completely nonspecific substances hardly give rise to the fluorescence restoration, and no significant differences to the blank signal (P values > 0.5 for all cases) are vested in their recovery ratios. Therefore, our sensing method possesses an admirable specificity for discriminating single-base variation to confront with the upcoming cell application.

Having confirmed the extracellular assay performance of PDA, the corresponding analytical indicators using a PDA@ZIF-8-supported fluorescent biosensor are also evaluated under the optimal dissociation pH value (Figure S12A). As expected, by virtue of the very effective PDA discharge event to ensure the working capacity of our amplifier, there are no obvious changes in the Cy3 fluorescence recovery (Figure S12B), the linear operating curve (Figure S12C, where the LOD is determined as 2.7 pM), and the specificity (Figure S12D) from that of the usage of pure PDA. These results reveal that the ZIF-8 encapsulation design can perfectly retain a favorable sensing ability.

Prior to actualizing this task of intracellular application, a methyl thiazolyl tetrazolium test is carried out to ascertain the underlying cytotoxicity of 365 nm UV light irradiation and PDA@ZIF-8. As shown in Figure S13A, thanks to the employment of the relatively mild power density, the viabilities of both cells can always be maintained at a very high range, even though the irradiation time is continued up to 20 min (wherein the cell viabilities are approaching to 90%). Beyond that, benefiting from the low toxic element composition of the ZIF-8 framework,[39] both the nanocomposite concentration (Figure S13B) and the incubation time (Figure S13C) do not show a conspicuous adverse effect on the cell growth. To further demonstrate the cell entry pathway of PDA@ZIF-8, we perform a colocalization imaging experiment (Figure S14), by which the signals of lyso tracker dye and Cy3 are completely overlapping, manifesting that the nanocomposites are indeed taken up by the cellular lysosome to enter into the cytoplasm. More importantly, the prominent distinctiveness in Cy3 signals before and after encapsulation of the PDA (Figure S15)

https://doi.org/10.1021/acs.analchem.1c04105
Anal. Chem. 2021, 93, 16638−16645

commendably attests a truth that the endocytosis efficiency is dramatically improved by means of the ZIF-8 delivery vehicle.

On the basis of the optimized incubation concentration (30 μg/mL, Figure S16) and time (4 h, Figure S17), the intracellular miRNA-196a imaging is finally achieved for two sorts of model living cancer cells (A549 and HeLa, wherein the secreted extracellular miRNAs do not impact the Cy3 signal recovery, Figure S18). As anticipated, when employing the silenced biosensor (in the absence of photoactivation), almost undetectable Cy3 fluorescence can be captured (bottom images in Figure 3A and B). Contrary to these unresponsive cases, the cells will give rise to very bright Cy3 signals upon treatment with the 365 nm UV light irradiation (top images in Figure 3A and B), indicating a resultful entropy-driven-induced sensing capacity in complicated specimens. Once the as-obtained confocal fluorescence images were quantified via a frequently applied ImageJ software to measure their gray levels (Figure S19A), it further arises that the fluorescence intensities of the light introduced groups are increased to approximately 8.5 times that of the untreated events (P values < 0.001 for both cells). Apart from this, we also discover that the average Cy3 emission of A549 cells is ∼1.4-fold higher than that of the HeLa cells. The recovery in different types of cancer cells is likely ascribed to the high-abundance nature of miRNA-196a in lung tissue-related tumors,[40] and such a content trend agrees well with the reverse transcription-polymerase chain reaction (RT-PCR) data (Figure S20). Furthermore, the imaging accuracies are confirmed by the flow cytometry analysis (Figure S19B), among which faultless consistence between these different detection means is presented.

In light of the potential role of miRNA-196a in the development of lung tumors, establishing an assay method with favorable sensitivity and specificity to precisely measure the intracellular levels at various physiological states can provide meaningful information for clinical diagnosis.[40] To this end, the A549 cells are treated with two forms of frequently used biochemical regulation reagents (250 nM miRNA mimic and 250 nM inhibitor), and the sensing of intracellular targets is further accomplished. As shown in Figure S21A, in comparison with the control cells (without any treatments, middle images), a dramatic signal enhancement is detected in the up-regulation group (top images), while the fluorescence intensity appears as a certain decline phenomenon for the down-regulating manner (bottom images). On the basis of the same quantitative procedures (Figure S21B), it arises that the Cy3 fluorescence of the former is enhanced by ∼3 times (P value < 0.01), and the latter accounts for ∼60% (P value < 0.01) of the untreated case, respectively. Likewise, flow cytometry (Figure S21C) and RT-PCR (Figure S22) experiments are implemented to collectively verify the imaging findings. Overall, our fluorescent biosensor can work as a powerful tracing tool in living biological systems.

CONCLUSIONS

Unlike the traditional entropy-driven amplifier, we have highlighted some innovative concepts in this work. First, the enzyme resistance of straight DNA probes is markedly enhanced by anchoring them onto the vertexes of dual DNA tetrahedrons. After encapsulating this fluorescent biosensor into ZIF-8 nanoparticles, we have proved that the endocytosis efficiency is significantly improved due to the effective elimination of the electrostatic repulsion of the cell membrane, and the perfect dissociation of this acid-sensitive delivery vehicle can availably discharge the internal sensing elements. To further boost the target identification, a PC-linker triggered photoresponsive sensing strategy is introduced, and this manner has brought about a completely manual operation process by making use of an externally mild 365 nm UV light source. Such a proposed photoresponsive increasing entropy event is collectively demonstrated by the thermokinetic calculation and a sequence of experimental means. By selecting miRNA-196a as the model target, the assay performance including linear relationship, sensitivity (LODs are 2.9 and 2.7 pM, respectively), and specificity is found to present negligible fluctuations before and after the ZIF-8 encapsulation. For the application of living cancer cells, our amplifier can realize a valid determination, and the imaging results agree well with other conventional approaches such as RT-PCR and flow cytometry. On the whole, our efforts can offer a brand-new biosensing notion and also a prospective diagnostic method for cancer medicine. Future attention will focus on the preparation of a targeted nanoprobe and also on the sensing of multiple biomarkers to identify specific cancer cell types.

ASSOCIATED CONTENT

Supporting Information

The Supporting Information is available free of charge at https://pubs.acs.org/doi/10.1021/acs.analchem.1c04105.

Reagents, PAGE procedures, thermokinetic calculation, extracellular detections, additional characterizations of PDA@ZIF-8, sensitivity and specificity, comparison of sensing sensitivity, cell viability, flow cytometry and RT-PCR, and prevalidation of intracellular imaging experiments (PDF)

AUTHOR INFORMATION

Corresponding Author

Cheng-Yu Li − *Hubei Province Key Laboratory of Occupational Hazard Identification and Control, School of Public Health, Medical College, Wuhan University of Science and Technology, Wuhan 430065, People's Republic of China*; orcid.org/0000-0003-4463-717X; Email: lichengyu@wust.edu.cn

Authors

Jia-Ling Gao − *Hubei Province Key Laboratory of Occupational Hazard Identification and Control, School of Public Health, Medical College, Wuhan University of Science and Technology, Wuhan 430065, People's Republic of China*

Liu Yuheng − *Hubei Province Key Laboratory of Occupational Hazard Identification and Control, School of Public Health, Medical College, Wuhan University of Science and Technology, Wuhan 430065, People's Republic of China*

Jun-Xian Liu − *Hubei Province Key Laboratory of Occupational Hazard Identification and Control, School of Public Health, Medical College, Wuhan University of Science and Technology, Wuhan 430065, People's Republic of China*

Hong-Wu Tang − *College of Chemistry and Molecular Sciences, Wuhan University, Wuhan 430072, People's Republic of China*; orcid.org/0000-0002-2258-6992

Complete contact information is available at: https://pubs.acs.org/10.1021/acs.analchem.1c04105

Author Contributions

§J.-L.G. and L.Y. contributed equally to this work.

https://doi.org/10.1021/acs.analchem.1c04105
Anal. Chem. 2021, 93, 16638−16645

Notes

The authors declare no competing financial interest.

■ ACKNOWLEDGMENTS

This work was supported by the National Natural Science Foundation of China (21904102, 21827808, and 81772256).

■ REFERENCES

(1) Jansson, M. D.; Lund, A. H. *Mol. Oncol.* **2012**, *6*, 590−610.
(2) Lin, S. B.; Gregory, R. I. *Nat. Rev. Cancer* **2015**, *15*, 321−333.
(3) Rupaimoole, R.; Slack, F. J. *Nat. Rev. Drug Discovery* **2017**, *16*, 203−221.
(4) Lee, H.; Lee, J.; Lee, S. G.; Doyle, P. S. *Anal. Chem.* **2020**, *92*, 5750−5755.
(5) Xia, Y. K.; Chen, T. T.; Zhang, L.; Zhang, X. L.; Shi, W. H.; Chen, G. Y.; Chen, W. Q.; Lan, J. M.; Li, C. Y.; Sun, W. M.; Chen, J. H. *Biosens. Bioelectron.* **2021**, *173*, 112834.
(6) Xue, S. Y.; Li, Q. Q.; Wang, L.; You, W. B.; Zhang, J.; Che, R. C. *Anal. Chem.* **2019**, *91*, 2659−2666.
(7) Liu, P.; Qian, X. Q.; Li, X. M.; Fan, L.; Li, X. Y.; Cui, D. X.; Yan, Y. R. *ACS Appl. Mater. Interfaces* **2020**, *12*, 45648−45656.
(8) Wen, Y. L.; Li, L. Y.; Li, J.; Lin, M. H.; Liu, G.; Liang, W.; Xu, L.; Li, Y.; Zuo, X. L.; Ren, S. Z.; Zhu, Y. *Anal. Chem.* **2020**, *92*, 4498−4503.
(9) Li, C. Y.; Kang, Y. F.; Qi, C. B.; Zheng, B.; Zheng, M. Q.; Song, C. Y.; Guo, Z. Z.; Lin, Y.; Pang, D. W.; Tang, H. W. *Anal. Chem.* **2019**, *91* (12), 7950−7957.
(10) Li, C. Y.; Zhang, T.; Kang, Y. F.; Qi, C. B.; Zheng, B.; Xu, C. M.; Lin, Y.; Pang, D. W.; Tang, H. W. *Chem. Commun.* **2020**, *56* (51), 6997−7000.
(11) Meng, X. D.; Zhang, K.; Yang, F.; Dai, W. H.; Lu, H. T.; Dong, H. F.; Zhang, X. J. *Anal. Chem.* **2020**, *92* (12), 8333−8339.
(12) Li, Q.; Zhou, S. H.; Zhang, T.; Zheng, B.; Tang, H. W. *Biosens. Bioelectron.* **2020**, *150*, 111866.
(13) Zhang, J.; He, M. Y.; Nie, C. P.; He, M. M.; Pan, Q. S.; Liu, C.; Hu, Y. L.; Yi, J. T.; Chen, T. T.; Chu, X. *Anal. Chem.* **2019**, *91*, 9049−9057.
(14) Li, D. X.; Zhang, T. T.; Yang, F.; Yuan, R.; Xiang, Y. *Anal. Chem.* **2020**, *92*, 2074−2079.
(15) Chen, J. Y.; Wu, Y.; Fu, C. C.; Cao, H. Y.; Tan, X. P.; Shi, W. B.; Wu, Z. Y. *Biosens. Bioelectron.* **2019**, *143*, 111619.
(16) Cui, L.; Zhou, J. H.; Yang, X. Y.; Dong, J.; Wang, X. L.; Zhang, C. Y. *Chem. Commun.* **2020**, *56*, 10191−10194.
(17) Wang, L.; Liu, P. F.; Liu, Z. J.; Zhao, K. R.; Ye, S. Y.; Liang, G. X.; Zhu, J. J. *ACS Sensors* **2020**, *5*, 3584−3590.
(18) Liang, C. P.; Ma, P. Q.; Liu, H.; Guo, X. G.; Yin, B. C.; Ye, B. C. *Angew. Chem., Int. Ed.* **2017**, *56* (31), 9077−9081.
(19) Li, F. Y.; Li, G.; Cao, S. J.; Liu, B. S.; Ren, X. L.; Kang, N.; Qiu, F. *Biosens. Bioelectron.* **2021**, *172*, 112757.
(20) Li, Y.; Huang, C. Z.; Li, Y. F. *Anal. Chem.* **2019**, *91*, 9308−9314.
(21) Lv, M. M.; Wu, Z.; Yu, R. Q.; Jiang, J. H. *Chem. Commun.* **2020**, *56*, 6668−6671.
(22) Oishi, M.; Juji, S. *ACS Appl. Mater. Interfaces* **2021**, *13*, 35533−35544.
(23) Chen, A. K.; Behlke, M. A.; Tsourkas, A. *Nucleic Acids Res.* **2007**, *35*, e105.
(24) Tay, C. Y.; Yuan, L.; Leong, D. T. *ACS Nano* **2015**, *9*, 5609−5617.
(25) Jia, R. C.; He, X. X.; Ma, W. J.; Lei, Y. L.; Cheng, H.; Sun, H. H.; Huang, J.; Wang, K. M. *Anal. Chem.* **2019**, *91*, 15107−15113.
(26) Lin, Q.; Wang, A. M.; Liu, S. Y.; Li, J.; Wang, J. L.; Quan, K.; Yang, X. H.; Huang, J.; Wang, K. M. *Chem. Commun.* **2020**, *56*, 5303−5306.
(27) Zhang, R. Y.; Zhang, R. X.; Jiang, W.; Xu, X. W. *Chem. Commun.* **2021**, *57*, 2188−2191.
(28) Xu, C.; He, X. Y.; Peng, Y.; Dai, B. S.; Liu, B. Y.; Cheng, S. X. *Anal. Chem.* **2020**, *92*, 2088−2096.
(29) Mostakim, S. K.; Banesh, S.; Trivedi, V.; Biswas, S. *Inorg. Chem.* **2018**, *57*, 14574−14581.
(30) Wang, M. H.; Hu, M. Y.; Li, Z. Z.; He, L. H.; Song, Y. P.; Jia, Q. J.; Zhang, Z. H.; Du, M. *Biosens. Bioelectron.* **2019**, *142*, 111536.
(31) Yan, D.; Lou, Y. H.; Yang, Y. H.; Chen, Z.; Cai, Y. P.; Guo, Z. Y.; Zhan, H. B.; Chen, B. L. *ACS Appl. Mater. Interfaces* **2019**, *11*, 47253−47258.
(32) Shi, X. X.; Meng, H. M.; Geng, X.; Qu, L. B.; Li, Z. H. *ACS Sensors* **2020**, *5*, 3150−3157.
(33) Lubbe, A. S.; Szymanski, W.; Feringa, B. L. *Chem. Soc. Rev.* **2017**, *46*, 1052−1079.
(34) Zhao, J.; Gao, J. H.; Xue, W. T.; Di, Z. H.; Xing, H.; Lu, Y.; Li, L. L. *J. Am. Chem. Soc.* **2018**, *140*, 578−581.
(35) Chu, H. Q.; Zhao, J.; Mi, Y. S.; Zhao, Y. L.; Li, L. L. *Angew. Chem., Int. Ed.* **2019**, *58*, 14877−14881.
(36) Zhao, J.; Chu, H. Q.; Zhao, Y.; Lu, Y.; Li, L. L. *J. Am. Chem. Soc.* **2019**, *141*, 7056−7062.
(37) Lin, P. Y.; Yu, S. L.; Yang, P. C. *Br. J. Cancer* **2010**, *103*, 1144−1148.
(38) Gao, W. W.; Ku, W. L.; Pan, L. X.; Perrie, J.; Zhao, T. T.; Hu, G. Q.; Wu, Y. Z.; Zhu, J.; Ni, B.; Zhao, K. J. *Nucleic Acids Res.* **2021**, *49*, e56.
(39) Luo, Z. D.; Fan, S. R.; Gu, C. Y.; Liu, W. C.; Chen, J. X.; Li, B. H.; Liu, J. A. *Curr. Med. Chem.* **2019**, *26*, 3341−3369.
(40) Xiong, M. Q.; Wang, P.; Pan, B.; Nie, J. J.; Wang, S. K.; He, B. S. *Biosci. Rep.* **2021**, *41*, BSR20203559.

https://doi.org/10.1021/acs.analchem.1c04105
Anal. Chem. 2021, 93, 16638−16645